

Static Wind Tunnel Testing of a Legged Venus Lander

Clara O'Farrell*, Graham E. Merrifield†, Jason Rabinovitch‡

Jet Propulsion Laboratory, California Institute of Technology, Pasadena, CA, 91109, USA

A static wind tunnel test was conducted to determine the static aerodynamic coefficients of the surface lander design proposed by the Venus In-Situ Atmospheric and Geochemical Explorer (VISAGE). The baseline design of the lander consists of a spherical pressure vessel with a top-mounted circular drag plate for aerodynamic deceleration, and three fixed landing legs. A modular subscale lander model, which allowed testing of several drag plate and landing leg configurations, was fabricated using rapid-prototyping techniques. The model was tested with four different drag plates and three different leg configurations, at a dynamic pressure of 1610 Pa and Mach number of 0.15. Testing was conducted using legs of varying diameter in order to determine the appropriate scaling of the results to Reynolds numbers representative of terminal descent at Venus. The static aerodynamic force (axial, normal, and side), and moment (rolling, pitching, yawing) coefficients for each lander configuration were determined as a function of model orientation. All model configurations were found to be statically stable in the range of total angles of attack considered (0 to 30 deg). However, the drag performance and degree of static stability of the model were dependent on the dihedral angle of the circular drag plate. The results will enable the creation of a preliminary aerodatabase for the VISAGE lander concept, and allow the effect of design changes on aerodynamic performance to be evaluated.

Nomenclature

A	Cross-sectional area of tunnel test section
AF	Axial force on the lander
C_A	Axial force coefficient
C_D	Lander drag coefficient
C_N	Normal force coefficient
C_Y	Side force coefficient
$C_{l,PV}$	Rolling moment coefficient at the pressure vessel center
$C_{m,PV}$	Pitching moment coefficient at the pressure vessel center
$C_{n,PV}$	Yawing moment coefficient at the pressure vessel center
D_0	Diameter of the pressure vessel without exterior insulation
D_P	Drag plate diameter
D_S	Payload sphere diameter (with exterior insulation)
d_{legs}	Diameter of the lander model legs
F_D	Lander drag force
L_{legs}	Length of the lander model legs
NF	Normal force on the lander
PM	Pitching moment about the center of the pressure vessel
q_c	Blockage-corrected dynamic pressure
q_∞	Freestream dynamic pressure
RM	Rolling moment about the center of the pressure vessel
S_0	Projected area of the pressure vessel without exterior insulation
SF	Side force on the lander

*Guidance and Control Engineer, AIAA Member

†Undergraduate Student

‡Mechanical Engineer, AIAA Member

u, v, w	Flow velocity in the lander coordinate system
V_∞	Freestream velocity
X, Y, Z	Axes of the lander coordinate system
YM	Yawing moment about the center of the pressure vessel
α	Model angle of attack
α_T	Model total angle of attack
β	Model angle of sideslip
Γ	Drag plate dihedral
ν	Kinematic viscosity
ϕ	Model roll angle
ϕ_{α_T}	Total angle of attack clocking angle
θ	Turntable angle
DAS	Data Acquisition System
LWT	Lucas Wind Tunnel
SAGE	Surface and Atmosphere Geochemical Explorer
VISAGE	Venus In-Situ Atmospheric and Geochemical Explorer

I. Introduction

ALTHOUGH Venus is our closest planetary neighbor, much remains unknown about its surface and atmosphere. In the 1990's NASA's Magellan orbiter mapped the surface of Venus using synthetic aperture radar,¹ while the European Space Agency's Venus Express spacecraft studied the planet's atmosphere and surface by radio sounding and spectrometry from 2006 to 2015.² However, the last NASA mission to send a probe into the Venusian atmosphere was Pioneer-Venus in the late 1970s,³ while the last successful Venus surface sample measurement was made by the Soviet VEGA 1 mission in the mid-1980s.⁴ Thus, future missions to the surface of Venus will likely result in groundbreaking scientific discoveries and Venus mission concepts have featured prominently in the most recent Planetary Decadal Survey. As a result, several Venus missions have been proposed to NASA's New Frontiers and Discovery programs in recent years.

In the framework of the most recent New Frontiers cycle, the Venus In-Situ Atmospheric and Geochemical Explorer (VISAGE) mission concept is proposing to place a legged lander on the surface of Venus. The spacecraft would measure atmospheric composition at different altitudes during its descent to the surface, and the lander would be equipped with drills and instrumentation to conduct composition measurements at the surface. In addition, science cameras on the lander would capture high-resolution imagery during descent and on the surface. The mission's baseline design calls for the lander to separate from the parachute 55 km above the surface of Venus, free fall, and impact the surface at a velocity of approximately 9 m/s. The lander would be equipped with a rigid drag plate which allows it to achieve the desired descent rate, as well as with crushable material in the legs for impact attenuation. During descent, the lander must meet certain pitching and yawing stability requirements to avoid tumbling and allow the science cameras to acquire images during descent.

In late 2016, the VISAGE lander design team carried out a wind tunnel test campaign to determine the static aerodynamic characteristics of a subscale model of the preliminary lander design. The test was very similar to that carried out by the Venus Surface and Atmosphere Geochemical Explorer (SAGE) in 2010,⁵ and took place between November 28 and December 5, 2016 at the California Institute of Technology's (Caltech) Lucas Wind Tunnel (LWT). The principal goals of the test were to collect the drag and static aerodynamic data necessary to inform the selection of a final lander design that met the project's requirements, and to characterize the descent rate and static aerodynamics of the full-scale lander for use in flight dynamics simulations.

To achieve these objectives a modular lander model was constructed which allowed the testing of several drag plate and landing leg configurations. The wind tunnel model was a 8.6% scale model of the VISAGE preliminary design. The model was mounted to a sting on a turntable in the floor of the wind tunnel test section, which allowed the testing of the model at several orientations with respect to the freestream flow. A six-component force/torque sensor allowed measurements of the total aerodynamic forces and moments on the lander model. Data were obtained for four drag plate configurations and three leg configurations, at a single (subsonic) flow condition and a variety of model orientations. These data were processed to yield

drag, static aerodynamic force (axial, normal, and side), and moment (rolling, pitching, yawing) coefficients for each lander configuration.

This paper describes the test setup, operating conditions, test matrices, analyses, and results of the 2016 static wind tunnel test of the preliminary VISAGE lander design. It is organized as follows. Section II describes the configuration and execution of the wind tunnel test. Section III describes the methods used to analyze the results of the test, which are presented in Section IV. Finally, concluding remarks are provided in Section V.

II. Test Configuration and Execution

A. Lander Models

A subscale model of the preliminary VISAGE lander design was 3D-printed using ABS-M30 thermoplastic (Stratasys, Inc). Figure 1 shows the configuration of the legged lander model. The model was built to 8.6% scale, based on the outer diameter of the payload sphere including exterior insulation. In the resulting model, the payload sphere had an outer diameter of 11.4 cm. The remaining dimensions of the wind tunnel model are listed in Figure 1. The design of the model was modular, to allow the testing of several drag plate configurations in conjunction with the payload sphere. The following aspects of the drag plate design were varied:

- Dihedral angle (Γ). Drag plates with dihedral angles of 0 deg, 10 deg, and 30 deg were tested. The projected diameter of the plates (D_P) was kept constant.
- Solidity. The drag plate solidity was defined as the ratio of the solid area of the plate to the plate projected area. The size of the open area at the center of the drag plate was varied to obtain models with a solidity of 83% and 87%.

In addition, the models were tested with three lander leg configurations:

- No lander legs.
- Lander legs with tube outer diameter scaled geometrically from the full-scale VISAGE preliminary design, henceforth referred to as the “large legs”. The large legs were 3D-printed using the thermoplastic material used for the pressure vessel and drag plates (Figure 2(a)).
- Lander legs with tube outer diameter scaled to approximately 40% of the size required for geometric similarity, in order to estimate the effect of Reynolds number on aerodynamic forces on the legs as described in Section IV.C. These smaller leg tubes were assembled using aluminum wire soldered to a triangular leg plate which interfaced to the model payload sphere (Figure 2(b)). These are henceforth referred to as the “small legs.”

The diameter of all drag plate configurations was 25 cm, which accounts for less than 2% of the cross-sectional area of the wind tunnel test section. The blockage from the model increased the local dynamic pressure at the location of the model by approximately 5%.

B. Test Setup

The test was conducted at the LWT at Caltech. The test section of the tunnel is 1.3 m tall by 1.8 m wide by 7.5 m long, and features a floor turntable which can be rotated up to 90 deg clockwise and counter-clockwise. The setup for the wind tunnel test is shown in Figure 3. The test setup was similar to that used during prior wind tunnel testing conducted by the SAGE project.⁵ The model was mounted horizontally at the tunnel centerline, with the lander legs facing upstream, by means of an L-sting. The L-sting was mounted on the wind tunnel turntable, and the turntable was rotated so that testing could be conducted at a number of turntable angles (θ). A streamlined fairing was installed around the vertical strut of the L-sting to minimize aerodynamic forces on the test fixture. To limit model vibrations, the top section of the test fixture was secured to the turntable using a pair of guy wires tightened using turnbuckles.

An ATI Industrial Automation Mini45 Force/Torque sensor⁶ was used to record the forces and moments on the model at a rate of 100 Hz. The sensor was placed at the interface of the lander model and L-sting. The

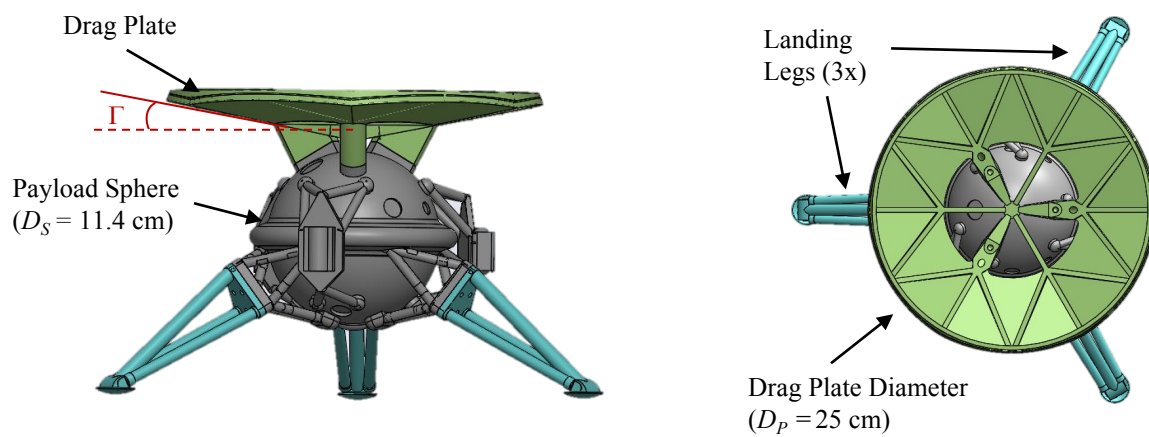


Figure 1. Lander model configuration and principal dimensions.

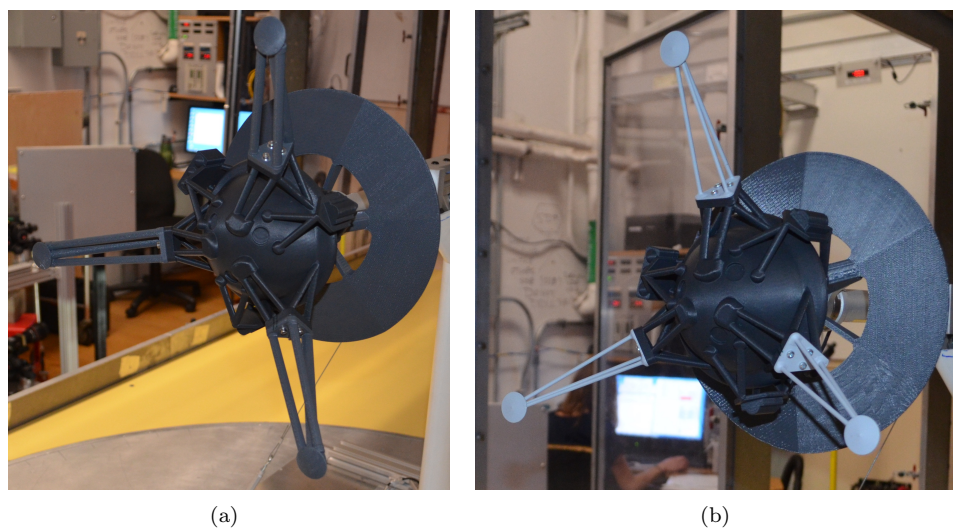


Figure 2. 3-D-printed lander model. (a) Large legs. (b) Small legs.

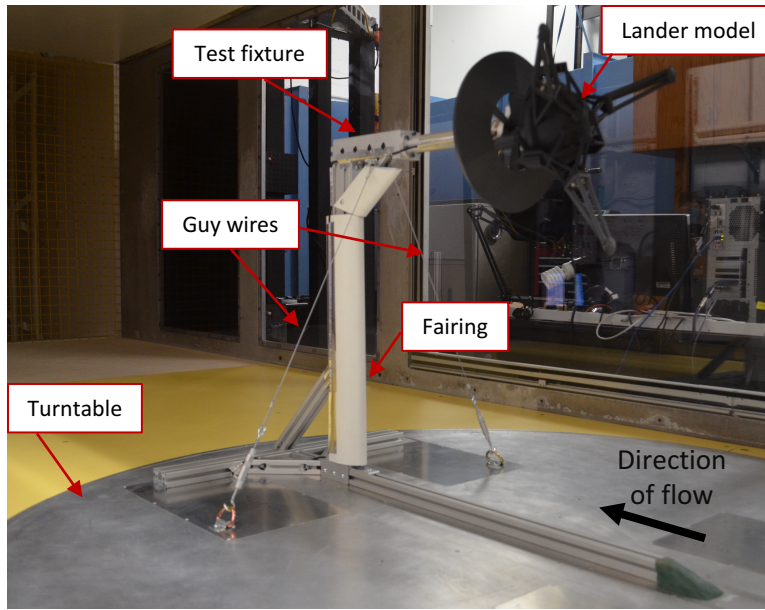


Figure 3. VISAGE test setup, including the aerodynamic fairing and guy wires.

sensor interfaced with the lander model and test fixture by means of specially-designed aluminum interface plates. On the test fixture side, the sensor interface plate was secured to the horizontal sting by means of 18 fasteners in a symmetrical pattern. This arrangement allowed the lander model to be rotated about its axis of symmetry in 20 deg increments, so that models could be tested at several roll angles (ϕ).

Tunnel operating conditions were recorded using the LWT's built-in instrumentation and Data Acquisition System (DAS). The following quantities were monitored for each test condition: dynamic pressure (in Pa), static pressure (Pa), temperature (K), tunnel speed (m/s). Data was acquired at 100 Hz, and reported for a sample time of 20 sec at each test condition.

Tests were conducted at an approximate wind speed of 51 m/s, approximately 80% of the LWT's maximum speed. This speed was selected in order to maximize the Reynolds number and the aerodynamic forces and moments on the model, while reducing the vibrations of the test fixture to an acceptable level. At this windspeed, the blockage-corrected dynamic pressure and Mach number in the tunnel were approximately 1610 Pa and 0.15, respectively. The Reynolds number based on the diameter of the drag plate was approximately 8.5×10^5 . The Reynolds numbers achieved during testing were between 15 and 60 times lower than those expected during the final descent phase of the VISAGE lander, following separation from the parachute. The proper scaling of the test results to conditions relevant to terminal descent at Venus is discussed in Section IV.C.

C. Test Matrix

A total of 12 model configurations were tested during the campaign. These configurations are listed in Table 1. The test was conducted in two phases. During the first phase, the configurations listed in Table 1 were tested at a fixed model roll angle of $\phi = -2 \text{ deg}^a$. The turntable was rotated, and the forces and moments on the model were recorded at different turntable angles (θ). For each configuration tested, turntable angle sweeps between -30 deg and 30 deg were performed. During Phase II, a subset of the configurations listed in Table 1 was tested while varying both the roll angle and turntable angle, to fully characterize the static aerodynamic characteristics of these configurations. For each configuration tested during Phase II, turntable

^aThe roll angle during Phase I was nominally set to 0 deg. However, exact alignment of the model axes with the tunnel was not possible. Using a set of calibrated weights, the offset in the roll angle was determined to be -2 deg. No appreciable offsets were determined about the remaining model axes. This offset in roll angle resulted in a departure from zero of the angle of sideslip (β) during Phase I. β ranged from -1 deg to 1 deg.

angle sweeps between -30 deg and 30 deg were performed at four roll angles.

Table 1. Model configurations tested.

Configuration ID	Drag Plate		Legs	Available Data
	Solidity	Γ (deg)		
1	83%	10	None	Phase I
2	83%	10	Small	Phase I, Phase II
3	83%	10	Large	Phase I, Phase II
4	87%	10	None	Phase I
5	87%	10	Small	Phase I
6	87%	10	Large	Phase I
7	83%	0	None	Phase I
8	83%	0	Small	Phase I
9	83%	0	Large	Phase I
10	83%	30	None	Phase I
11	83%	30	Small	Phase I
12	83%	30	Large	Phase I

III. Data Analyses

A. Coordinate Systems and Angles

The aerodynamic forces and moments measured by the force/torque sensor were transformed to the lander body coordinate system illustrated in Figure 4. The origin of the coordinate system was located at the center of the lander's spherical pressure vessel. The X axis runs along the axis of symmetry of the lander, pointing forwards (towards the lander legs). The Y axis is perpendicular to the X axis as indicated in Figure 4. The Z axis is orthogonal to the X and Y axes, such that the three axes form a right-handed coordinate system.

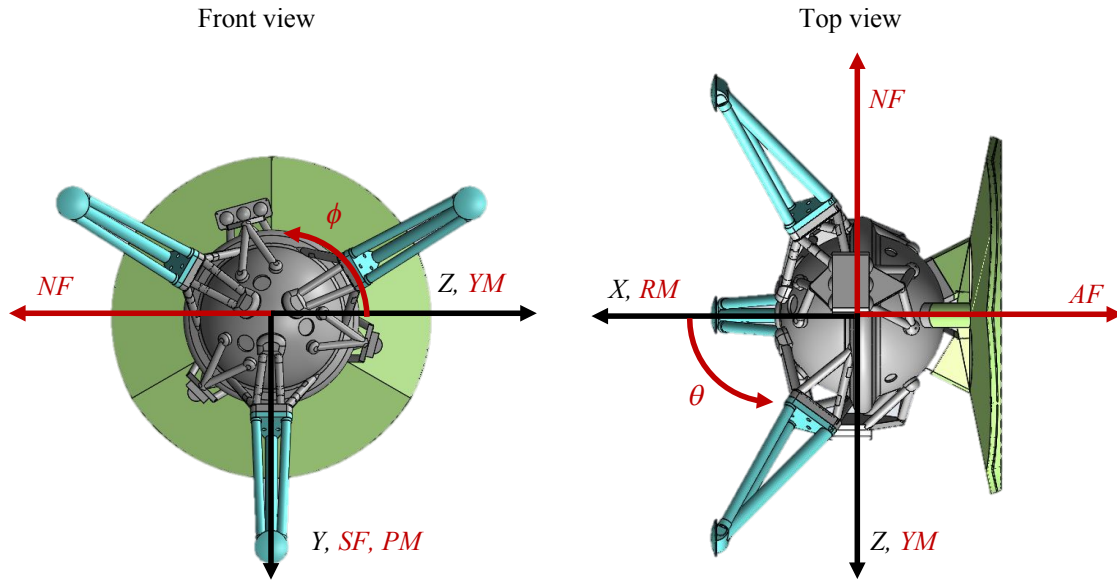


Figure 4. Body-centered coordinate system.

The positive direction of the roll angle (ϕ) and turntable angle (θ) are also shown in Figure 4. The turntable angle is zero when the X axis on the lander body coordinate system points directly upstream, and θ is positive when the turntable is rotated in the counterclockwise direction as defined by an observer within the test section. When the model is not rolled ($\phi = 0$ deg), the turntable angle (θ) is equivalent to the negative of the model angle of attack ($-\alpha$). The standard definitions for the axial (AF), normal (NF), and side (SF) forces, and the pitching (PM), yawing (YM), and rolling (RM) moments about the body coordinate system are also shown in Figure 4.

The components of velocity (u, v, w) and the wind angles ($\alpha, \beta, \alpha_T, \phi_{\alpha_T}$) were defined in the body coordinate system from the freestream velocity (V_∞), turntable angle (θ), and roll angle (ϕ) using the following equations:

$$u = V_\infty \cos \theta \quad (1)$$

$$v = -V_\infty \sin \theta \sin \phi \quad (2)$$

$$w = -V_\infty \sin \theta \cos \phi \quad (3)$$

$$\alpha = \arctan\left(\frac{w}{u}\right) = \arctan(-\tan \theta \cos \phi) \quad -\pi < \alpha \leq \pi \quad (4)$$

$$\beta = \arcsin\left(\frac{v}{V_\infty}\right) = \arcsin(-\sin \theta \sin \phi) \quad -\frac{\pi}{2} < \beta \leq \frac{\pi}{2} \quad (5)$$

$$\alpha_T = \arccos\left(\frac{u}{V_\infty}\right) = |\theta| \quad 0 \leq \alpha_T \leq \pi \quad \text{for } -\pi < \theta \leq \pi \quad (6)$$

$$\phi_{\alpha_T} = \arctan\left(\frac{v}{w}\right) \quad 0 \leq \phi_{\alpha_T} \leq 2\pi \quad (7)$$

B. Aerodynamic Coefficients

At the start of the test, the internal clocks on the computers recording the LWT and Mini45 force/torque sensor data streams were synchronized. These synchronized time stamps were used to time-align the 20-second-long records from the LWT and Mini45 sensors. The LWT and Mini45 results were then low-pass filtered at 5 Hz. At the start and end of each run, a data point was recorded with no flow in the tunnel. The two data points were used to tare the Mini45 sensor prior to each run and to correct for sensor drift. Any drift recorded in the sensor was assumed to be a linear function of time.

Once the measurements had been tared, filtered, and synchronized, the data from the LWT DAS were corrected for wind tunnel blockage effects^b. The aerodynamic force and moment coefficients were then calculated from:

$$C_A = \frac{AF}{q_c S_0} \quad (8)$$

$$C_N = \frac{NF}{q_c S_0} \quad (9)$$

$$C_Y = \frac{SF}{q_c S_0} \quad (10)$$

$$(11)$$

where q_c is the dynamic pressure corrected for wind tunnel blockage. The projected area of the pressure vessel without exterior insulation was selected as the reference area (S_0), as the dimensions of the payload were expected to remain the most constant throughout the lander design process. Note that this leads to aerodynamic coefficients whose magnitude is larger than that expected when a more conventional reference area (such as the drag plate area) is used. The rolling, pitching, and yawing moment coefficients about the

^bFollowing Maskell,⁷ disks of three different sizes were tested in the LWT and a model of the form: $q_c = \left(1 + k \frac{F_D}{A q_\infty}\right) q_\infty$ (where F_D is the measured drag force on the lander model, A is the tunnel cross-section, and q_∞ is the freestream dynamic pressure) was fit to the results. For the present configuration, it was found that $k = 2.78$.

center of the pressure vessel are given by:

$$C_{l,PV} = \frac{RM}{q_c S_0 D_0} \quad (12)$$

$$C_{m,PV} = \frac{PM}{q_c S_0 D_0} \quad (13)$$

$$C_{n,PV} = \frac{YM}{q_c S_0 D_0} \quad (14)$$

where the reference length (D_0) is the diameter of the pressure vessel without exterior insulation. The lander drag coefficient (C_D) was computed as:

$$C_D = \frac{AF \cos \theta - NF \sin \theta \sin \phi - SF \sin \theta \cos \phi}{q_c S_0} \quad (15)$$

The results from each 20-sec test point were averaged to obtain the mean forces, moments, flow conditions, and aerodynamic coefficients for each test point. For a subset of the configurations, roll angles, and turntable angles considered, repeated data points were collected. Where repeated data sets were available, these were averaged.

Figure 5 shows the aerodynamic force and moment coefficients as a function of angle of attack for Configuration 2 in Table 1 (drag plate with 83% solidity, 10 deg dihedral, and the small-diameter landing legs). The data shown in Figure 5 correspond to a model tested with $\phi = -2$ deg. Over the range of turntable angles considered, β ranges from -1 deg to 1 deg. The error bars in Figure 5 represent estimates of the uncertainty in the measurements.^c Note that the uncertainties in C_Y , $C_{l,PV}$, and $C_{n,PV}$ in Figure 5 exceed the measured value of these quantities. This was not unexpected for the side force and yawing moment, as the values of C_Y and $C_{n,PV}$ were expected to be very small when the model was tested with negligible roll angle. As discussed in Section IV.E, we were able to determine C_Y and $C_{n,PV}$ at non-zero roll angles. However, we were unable to resolve the static rolling moment coefficient at any test condition. As expected, the values of C_A are largely symmetric about the $\alpha = 0$ axis, while the C_N and $C_{m,PV}$ are anti-symmetric about this axis.

IV. Results

A. Drag Coefficient at 0 deg

Table 2 presents a summary of the average drag coefficient at 0 deg angle of attack, for all model configurations tested during Phase I. The results listed in the table correspond to models tested with a roll angle of -2 deg. Several trends are apparent from these results, which are also shown graphically in Figure 6. As expected, leg configuration has a significant effect on drag at $\alpha = 0$ deg. For all drag plates considered, the C_D of the model increased as the diameter of the model legs was increased. However, the magnitude of this increase varied from configuration to configuration. The proper scaling of the results for the different leg configurations is discussed in Section IV.C.

In addition, there is no appreciable difference between the C_D at $\alpha = 0$ deg of the configuration with 10 deg dihedral and 83% solidity, and the configuration with the same dihedral and 87% solidity. This is consistent with the observations made during smoke visualization tests that, when the lander model is placed at an angle of attack of 0 deg, there is no appreciable flow through the opening at the center of the drag plate (Figure 7). At larger angles of attack, it is expected that there will be flow through the open area at the center of the drag plate. The effect of drag plate solidity on the aerodynamic performance of the lander at non-zero angles of attack is discussed in the next subsection.

Finally, the increasing the dihedral angle of the drag plate results in a decrease in the drag coefficient at $\alpha = 0$ deg, for all lander leg sizes. The effect of dihedral angle on the lander's force and moment coefficients is described in Section IV.D.

^cThe bias and precision uncertainties were estimated for all aerodynamic coefficients. Throughout the text, the total uncertainty estimates are stated as a 95% confidence interval.

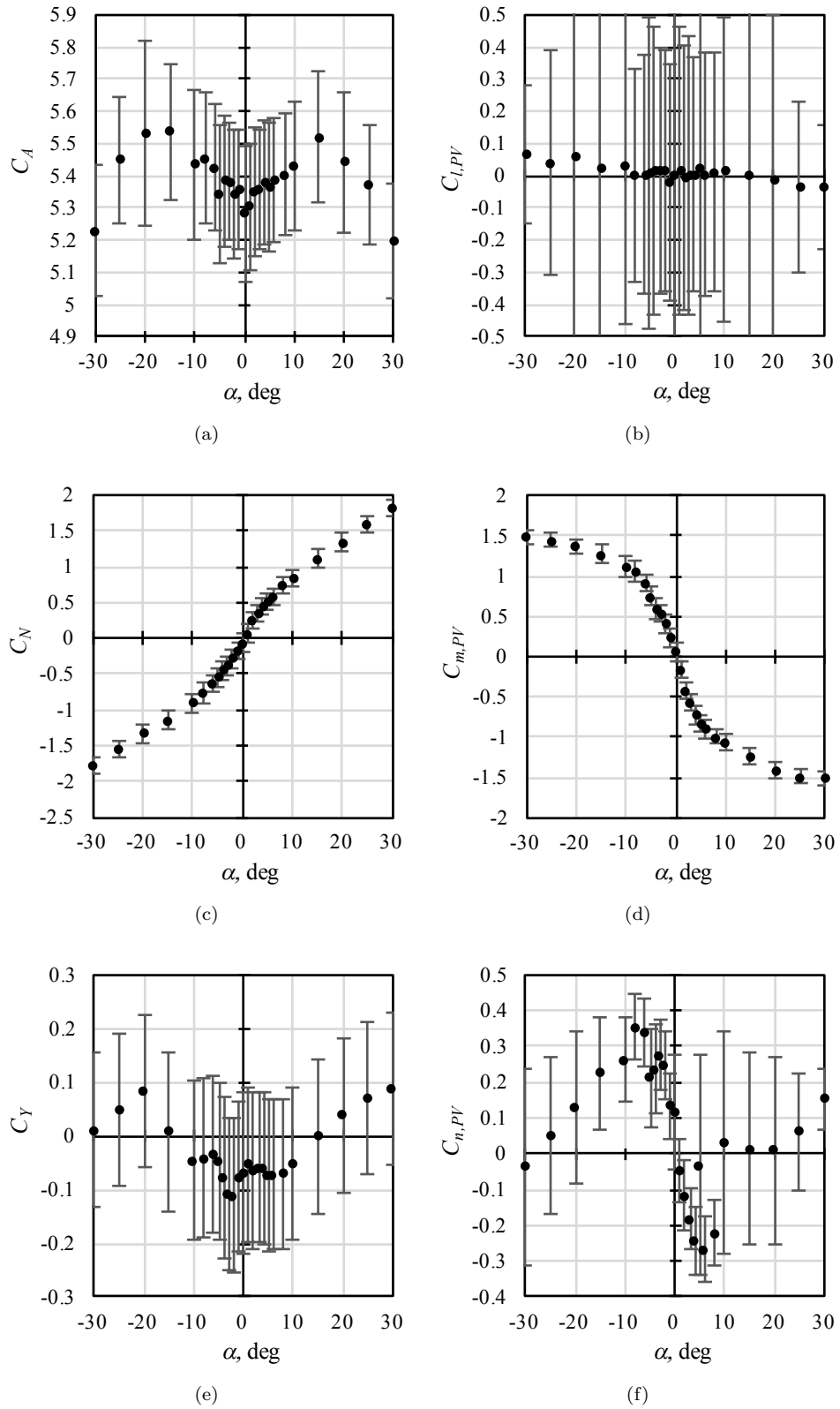


Figure 5. Aerodynamic force and moment coefficients for Configuration 2 (drag plate with 83% solidity, 10 deg dihedral, small lander legs). The error bars represent the total uncertainty in the measurements, as a 95% confidence interval.

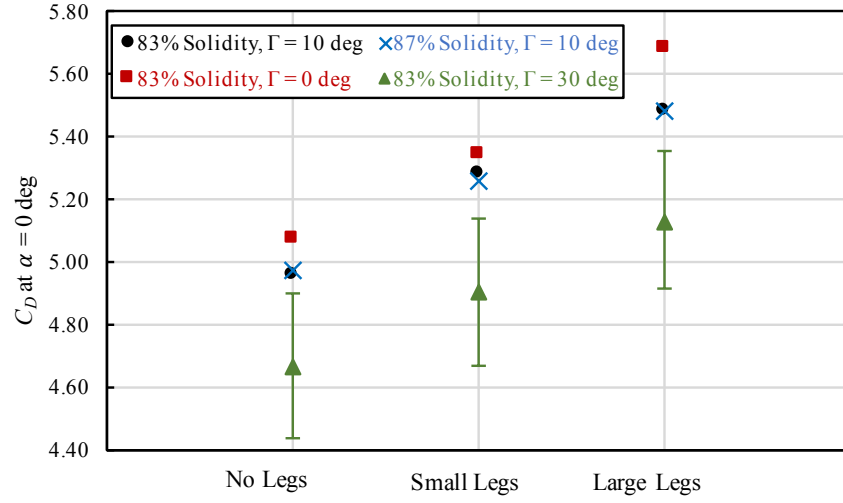


Figure 6. Effect of leg configuration on C_D at $\alpha = 0^\circ$. The error bars show the uncertainty on the results for a single drag plate configuration, for reference.

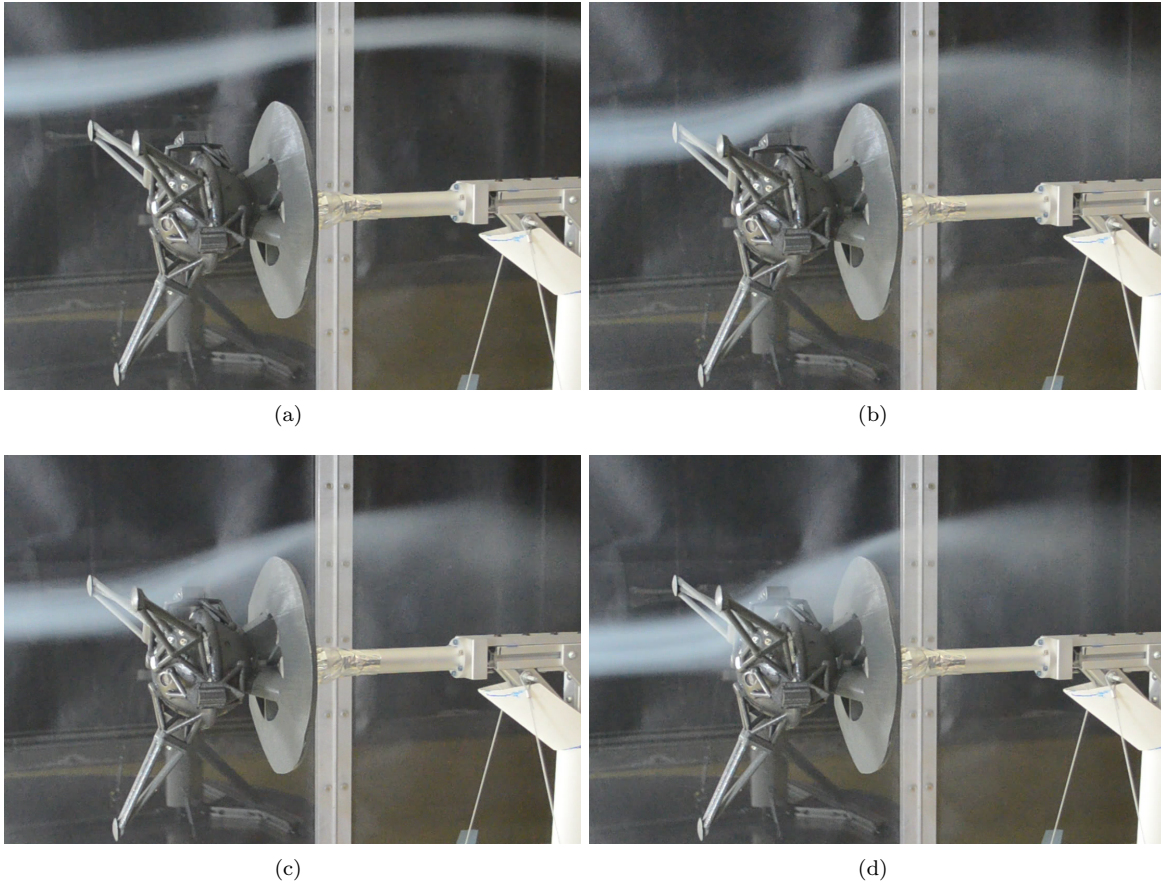


Figure 7. Streaklines generated using smoke visualization, illustrating that there is no appreciable flow through the opening at the center of the drag plate when the model has a 0° angle of attack.

Table 2. C_D at 0 deg angle of attack for all configurations tested during Phase I.

Configuration ID	Drag Plate		Legs	C_D
	Solidity	Γ (deg)		
1	83%	10	None	4.95 ± 0.19
2	83%	10	Small	5.28 ± 0.21
3	83%	10	Large	5.49 ± 0.20
4	87%	10	None	4.98 ± 0.24
5	87%	10	Small	5.26 ± 0.20
6	87%	10	Large	5.49 ± 0.25
7	83%	0	None	5.07 ± 0.18
8	83%	0	Small	5.35 ± 0.12
9	83%	0	Large	5.69 ± 0.19
10	83%	30	None	4.67 ± 0.23
11	83%	30	Small	4.91 ± 0.24
12	83%	30	Large	5.14 ± 0.22

B. Effect of Drag Plate Solidity

Figure 8 illustrates the effect of the size of the opening at the center of the drag plate on the aerodynamic coefficients of the lander at non-zero angles of attack. Figure 8(a) shows C_A vs. α for all configurations featuring a drag plate with a 10 deg dihedral (Configuration 1 through Configuration 6). Figure 8(b) shows the pitching moment coefficient curve for these same configurations. In both plots, the filled symbols represent the results for the drag plates with 83% solidity, while the open symbols represent the 87% solidity results. Configurations with the same leg size are shown using the same color. In each panel, error bars showing the total uncertainty (as a 95% confidence interval) for a single configuration (Configuration 1) are included for reference. The uncertainties on the remaining data points are comparable, and the corresponding error bars have been omitted for clarity.

For all leg sizes, there was very little difference between the C_A of the models with the 83% solidity plate and the 87% solidity plate near $\alpha = 0$ deg. At larger angles of attack, however, the C_A for the models with an 87% solidity plate became larger than those with the lower-solidity plate. This is likely caused by air flowing through the opening in the drag plates at larger angles of attack. The difference between the two plates was especially marked when the models were tested without any lander legs as: 1) the drag plate accounts for a larger fraction of the total aerodynamic forces in the absence of the legs, and 2) the absence of flow disturbances from the protruding legs highlights the differences arising from the flow through and around the drag plate. In contrast, the solidity of the drag plate does not appear to significantly affect the pitching moment coefficient, even at large angles of attack.

C. Reynolds Number Scaling

Figure 9 illustrates the effect of the lander leg size on the aerodynamic coefficients of the lander at non-zero angles of attack. Figure 9(a) shows C_A vs. α for the models featuring a drag plate with a 10 deg dihedral and 83% solidity, with the three different leg configurations (Configurations 1 to 3). Figure 9(b) shows the pitching moment coefficient curve for these same configurations. At all angles of attack, the axial force coefficient of the lander increased when the lander legs were included in the model. Furthermore, the models tested with the large legs had higher axial force coefficients than the models tested with the small legs. At all angles of attack, the increase in C_A from adding the small lander legs to the model tested without legs was larger than the increase in C_A from switching from the small legs to the large legs. However, the magnitude of the change in C_A appeared to be dependent on angle of attack. This is likely because the contributions to C_A from the main components of the legs (the circular footpads and the cylindrical leg tubes) both vary with angle of attack.

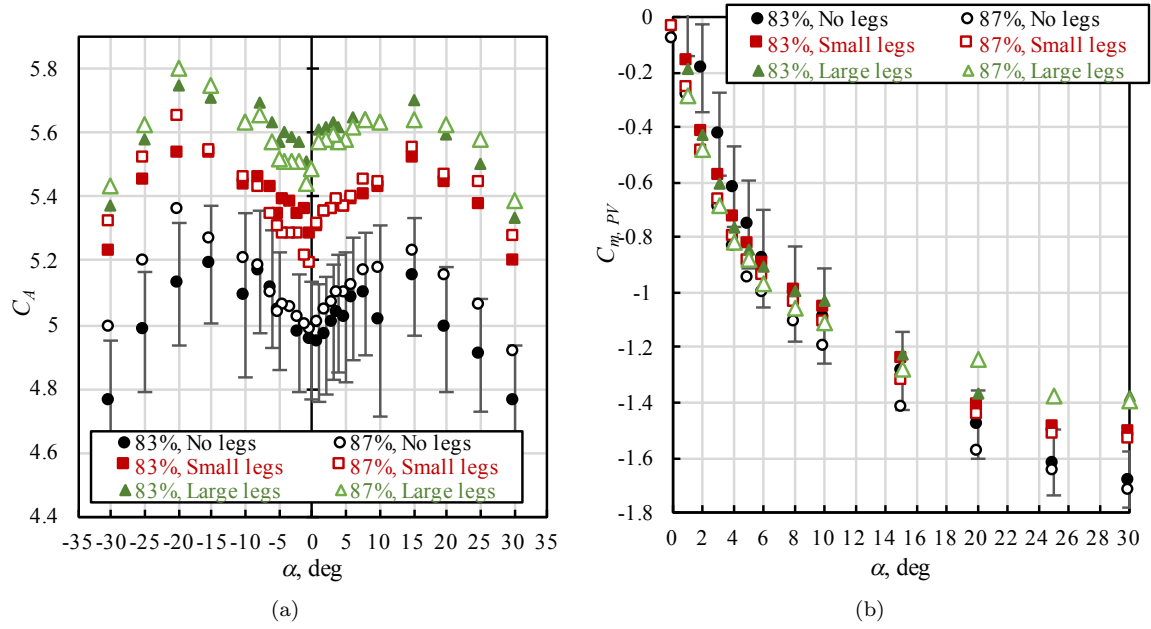


Figure 8. Axial force and pitching moment coefficients for the configurations including drag plates with a 10 deg dihedral and different solidities. Error bars showing the total uncertainty (as a 95% confidence interval) for Configuration 1 are shown for reference.

Figure 9(b) shows that the three lander models were statically stable about the pitching axis (whose origin is at the center of the payload sphere) at $\alpha = 0$ deg, regardless of leg configuration. However, the lander legs appear to have a de-stabilizing effect on the pitching dynamics of the lander. Lander models tested with the model legs showed a smaller restoring moment coefficient than the models tested without the legs. However, at total angles of attack below 20 deg or so, there was no significant difference in $C_{m,PV}$ between the models tested with the small and large legs.

The difference in the Reynolds number regime between the LWT test and terminal descent at Venus is particularly important for determining the influence of the legs on the aerodynamics of the lander. The legs are constructed from circular cylinders which, during vertical descent, are at approximately 60 deg to the flow. During terminal descent on Venus, the local Reynolds number at the legs (defined as $Re = V_\infty \cos \pi / 6 d_{legs} / \nu$ where V_∞ is the freestream flow velocity and ν is the kinematic viscosity) is expected to range from 4×10^5 to 1.5×10^6 . At these Reynolds numbers, the flow around a cylinder is supercritical, so the drag coefficient on the cylinder ranges from approximately 0.3 to 0.4.⁸ However, during testing the local Reynolds number for the geometrically-scaled (large) legs was in the subcritical range (on the order of 2.5×10^4). The drag coefficient of a cylinder at subcritical Reynolds numbers is approximately 1.2,⁸ so the drag coefficient measured on the large lander legs during the LWT testing is estimated to be approximately three to four times as large as expected during terminal descent at Venus.

However, the aerodynamic force on the cylindrical leg tubes is expected to scale with the frontal area of the tubes ($d_{legs} L_{legs}$). Since the diameter of the small model legs is approximately 40% that of the large legs, the small model legs are expected to generate approximately 40% of the aerodynamic force on the large legs. That is to say, the contribution to the measured lander drag coefficient from the large legs may be estimated as:

$$\Delta C_D = \frac{(C_D)_{\text{large}} - (C_D)_{\text{small}}}{(1 - 0.4)} \quad (16)$$

The contribution to C_D of the small legs may then be estimated to be 40% of ΔC_D , while the contribution to C_D from the supercritical flow about the full-scale lander legs at altitudes below 60 km on Venus may be estimated to be $\Delta C_D/4$. The drag coefficient of the lander during terminal descent on Venus may then be

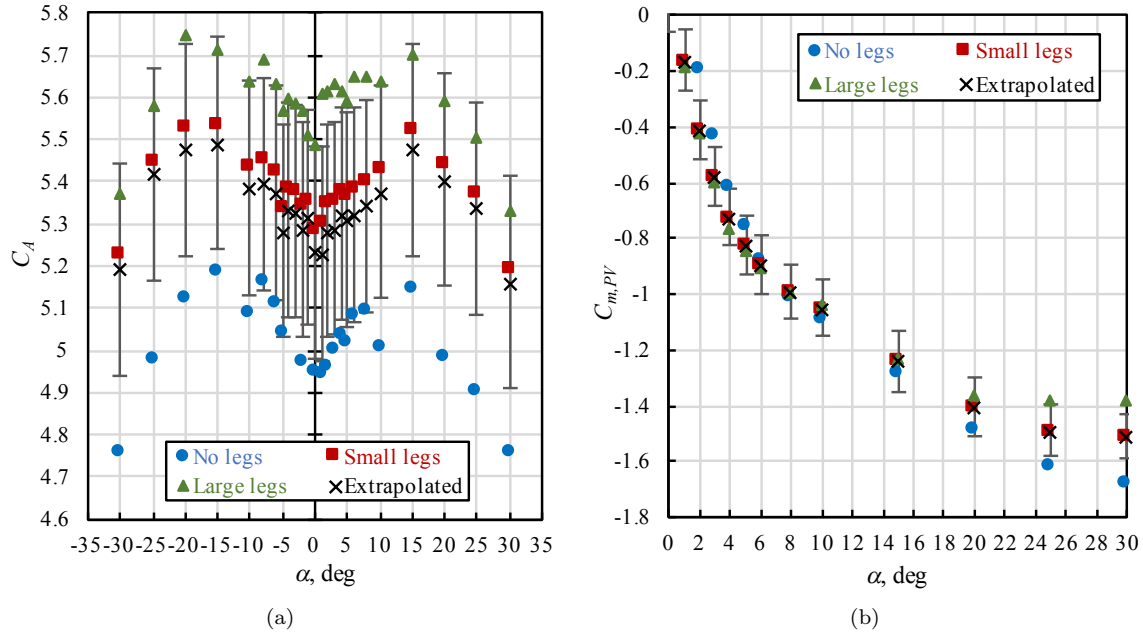


Figure 9. Axial force and pitching moment coefficients for the configurations including drag plates with a 10 deg dihedral and 83% solidity. The black crosses show the results of the extrapolation of coefficients to “at Venus” conditions. The error bars represent the total uncertainty on the extrapolated coefficients (at a 95% confidence interval).

estimated as:

$$(C_D)_{\text{Venus}} = (C_D)_{\text{small}} - 0.4\Delta C_D + 0.25\Delta C_D = (C_D)_{\text{small}} - \frac{(C_D)_{\text{large}} - (C_D)_{\text{small}}}{4} \quad (17)$$

The remaining model aerodynamic coefficients were extrapolated to “at Venus” conditions according to:

$$(C_A)_{\text{Venus}} = (C_A)_{\text{small}} - \frac{(C_A)_{\text{large}} - (C_A)_{\text{small}}}{4} \quad (18)$$

$$(C_N)_{\text{Venus}} = (C_N)_{\text{small}} - \frac{(C_N)_{\text{large}} - (C_N)_{\text{small}}}{4} \quad (19)$$

$$(C_Y)_{\text{Venus}} = (C_Y)_{\text{small}} - \frac{(C_Y)_{\text{large}} - (C_Y)_{\text{small}}}{4} \quad (20)$$

$$(C_{m,PV})_{\text{Venus}} = (C_{m,PV})_{\text{small}} \quad (21)$$

$$(C_{n,PV})_{\text{Venus}} = (C_{n,PV})_{\text{small}} \quad (22)$$

The extrapolated “at Venus” values of C_A and $C_{m,PV}$ for the model with the 83% solidity, 10 deg dihedral drag plate are denoted by the black crosses in Figure 9. For the moment coefficients, the values of $C_{m,PV}$ and $C_{n,PV}$ for the models tested with the small legs were used. At small angles of attack, the values of the moment coefficients for both leg sizes were too similar to allow proper extrapolation. At larger angles of attack, extrapolation was possible, but using the coefficients corresponding to the models with the small legs was deemed to be more conservative.

The drag coefficients at 0 deg angle of attack and “at Venus” conditions for the different drag plate configurations are shown in Table 3.

D. Drag Plate Dihedral

Figure 10 illustrates the effect of the drag plate dihedral the aerodynamic coefficients, extrapolated to terminal descent conditions at Venus. Figure 10(a) shows $(C_A)_{\text{Venus}}$ vs. α for the models featuring a drag

Table 3. C_D at 0 deg angle of attack, extrapolated to Reynolds numbers relevant to terminal descent at Venus.

Drag Plate Solidity	Drag Plate Dihedral (Γ)	$(C_D)_{\text{Venus}}$
83%	10 deg	5.23 ± 0.25
87%	10 deg	5.21 ± 0.30
83%	0 deg	5.26 ± 0.18
83%	30 deg	4.85 ± 0.23

plate with 83% solidity, with the three different dihedrals. Figure 10(b) shows the extrapolated pitching moment coefficient curve for these same configurations. In general, there is no significant difference between the axial force coefficients of the model with the flat drag plate and the model with 10 deg plate. However, the $(C_A)_{\text{Venus}}$ of the model with a 30 deg dihedral plate is significantly lower than that of the other two models at all angles of attack.

Figure 10(b) shows that the three lander models were statically stable about their pitching axis at $\alpha = 0$ deg, regardless of the drag plate dihedral. However, the model with the 30 deg dihedral plate experienced significantly larger restoring moments away from $\alpha = 0$ than the other two configurations. Unlike in Figure 10(a), there is a significant difference in the $(C_{m,PV})_{\text{Venus}}$ between the configurations with the flat and 10 deg drag plates. The model tested with the 0 deg drag plate had a consistently smaller restoring moment coefficient than the model with the 10 deg plate. It appears, therefore, that reducing the drag plate dihedral from 10 deg to 0 deg results in a moderate decrease in static pitching stability about the center of the payload sphere with little or no improvement in drag coefficient. However, the configuration with the 0 deg drag plate remains statically stable in the pitching direction, and a flat drag plate design may allow a larger drag plate to be accommodated inside the VISAGE entry capsule, thus improving overall drag performance.

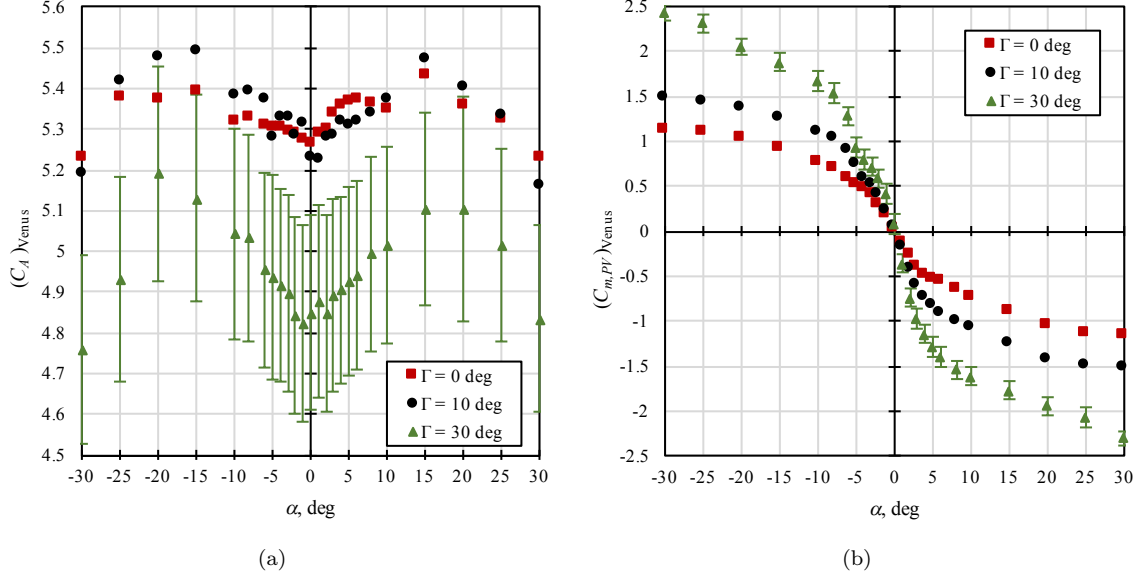


Figure 10. Extrapolated “at Venus” axial force and pitching moment coefficients for the drag plate configurations with 83% solidity and different dihedrals. Error bars showing the total uncertainty (as a 95% confidence interval) for a single configuration are shown for reference.

E. Roll Angle

During Phase II, force and moment data were recorded for two model configurations tested at four discrete roll angles and turntable angles ranging from -30 deg to 30 deg. The resulting data set spanned the total angle of attack (α_T) range from 0 deg to 30 deg, and included eight different α_T clocking angles: -2 deg, 18 deg, 38 deg, 58 deg, 178 deg, 198 deg, 218 deg, and 238 deg. The model configurations tested (Configuration 2 and Configuration 3) both featured the drag plate with 10 deg dihedral and 83% solidity, with different leg configurations (small vs large, respectively). Therefore, the Phase II results can be used to estimate the “at Venus” performance of the preliminary VISAGE lander design.

Figure 11 shows the axial force coefficient as a function of total angle of attack, for the preliminary lander design tested at the eight different α_T clocking angles. In each panel, error bars showing the total uncertainty (as a 95% confidence interval) for a single clocking angle are included for reference. The uncertainties on the remaining data points are comparable, and the corresponding error bars have been omitted for clarity. The curves of C_A as a function of α_T are quite similar for the different clocking angles. However, there are small differences between the curves which likely reflect the effect of the lander leg geometry as well as asymmetries in the lander body geometry.

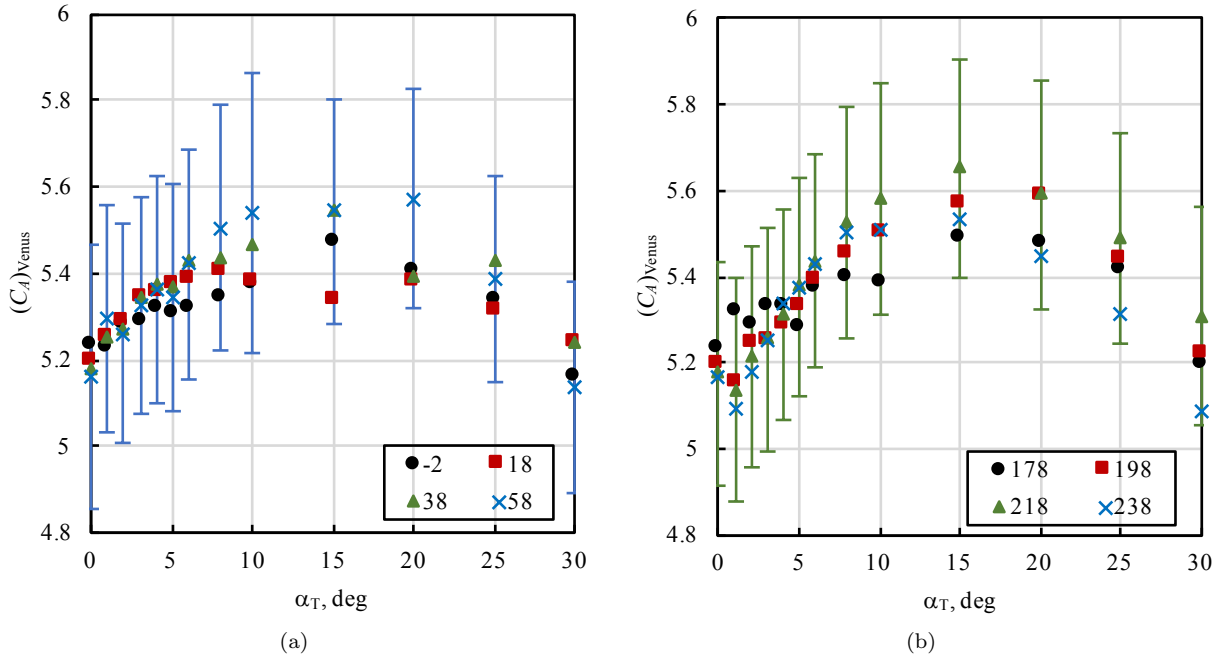


Figure 11. Extrapolated “at Venus” axial force coefficient for the baseline VISAGE lander (83% solidity and 10 deg dihedral) at different α_T clocking angles. Error bars showing the total uncertainty (as a 95% confidence interval) for a single clocking angle are shown for reference.

Figure 12 shows the magnitude of the non-axial force coefficients ($\sqrt{(C_N)_{\text{Venus}}^2 + (C_Y)_{\text{Venus}}^2}$) for the baseline lander model at the eight different α_T clocking angles. In each panel, error bars showing the total uncertainty (as a 95% confidence interval) for a single clocking angle are included for reference. The curves of the total normal force coefficient as a function of α_T are quite similar for the different clocking angles. Here again, small differences between the curves may reflect the effect of the lander leg geometry as well as asymmetries in the lander body geometry.

Figures 13 and 14 show the pitching and yawing moment coefficients for the baseline lander, at different α_T clocking angles. The pitching moment coefficient is shown as a function of angle of attack (α), while the yawing moment is shown as a function of angle of sideslip (β). Note that under the conventions selected for β and the yawing moment, a positive $(C_{n,PV})_{\text{Venus}}$ is stabilizing for $\beta > 0$. The results exhibit the expected symmetry, when the appropriate rotations are taken into account. For example, the $(C_{m,PV})_{\text{Venus}}$ vs. α for $\phi_{\alpha_T} = 18$ deg is very similar to the curve of $-(C_{n,PV})_{\text{Venus}}$ vs. β for $\phi_{\alpha_T} = 58$ deg. No large asymmetries

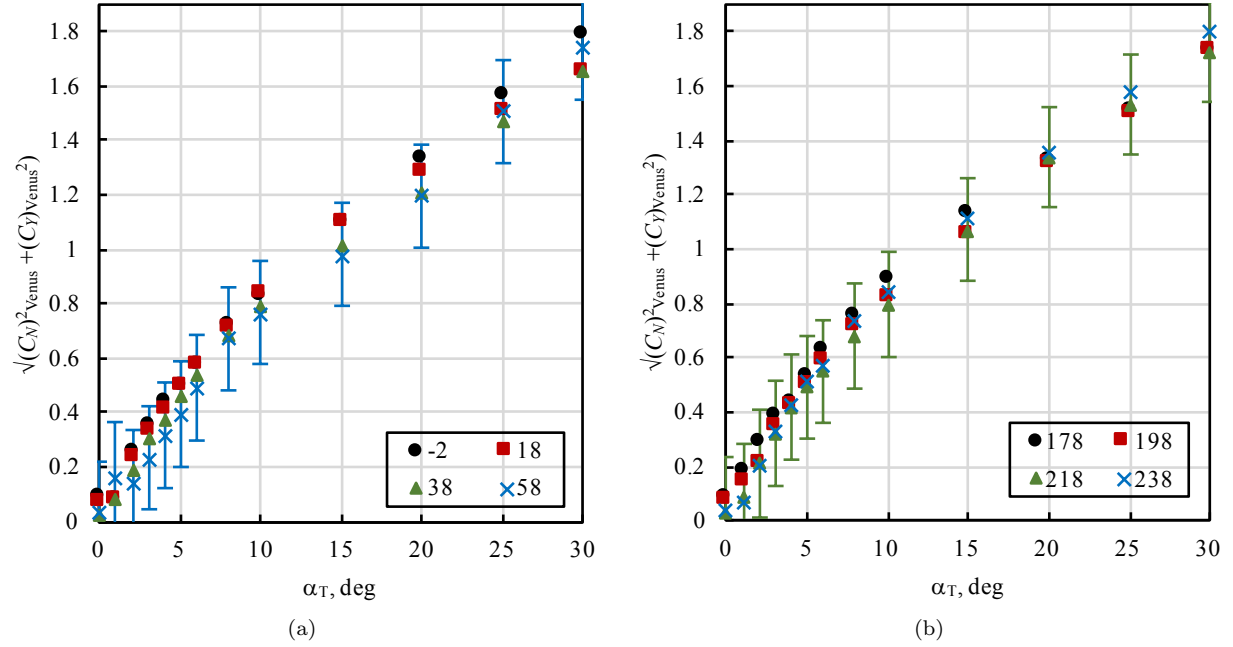


Figure 12. Extrapolated $\sqrt{(C_N)^2_{\text{Venus}} + (C_Y)^2_{\text{Venus}}}$ for the baseline VISAGE lander (83% solidity and 10 deg dihedral) at different α_T clocking angles. Error bars showing the total uncertainty (as a 95% confidence interval) for a single clocking angle are shown for reference

were identified in the aerodynamic coefficients, which suggests that the results obtained at $\phi = -2$ deg during Phase I are sufficient for developing a preliminary database of static aerodynamic performance for all the configurations considered.

V. Summary and Conclusions

In the late fall of 2016, a set of candidate configurations for the VISAGE Venus lander mission concept were tested at the Caltech LWT. The test was conducted in two phases. In the first phase, the static aerodynamic force and moment coefficients of 12 candidate configurations were determined at a range of angles of attack (-30 deg to 30 deg) but at a single model roll angle. During Phase II, two configurations were tested at a series of model roll angles to obtain static aerodynamic coefficients at a variety of angles of attack and angles of sideslip. The model configurations included four different drag plate designs, and three leg configurations.

For all configurations, the static rolling moments on the lander model could not be determined given the resolution of the sensor and the fluctuations in the measurements. However, the axial, normal, and side force coefficients and the pitching and yawing moment coefficients of the lander were obtained for all configurations. This allowed the lander design team to evaluate the static aerodynamic performance of the different model configurations.

Lander models with three different configurations were tested: with no legs, as well as with legs of two different diameters. The results obtained from the three leg configurations allow the contributions to the static aerodynamic forces of the pressure vessel and drag plate to be separated from those of the landing legs. Thus, the aerodynamic effect of configuration changes to the three main components of the lander can be evaluated. In addition, comparing the results obtained using models with legs of different diameter allowed us to determine the appropriate scaling of the results obtained in the wind tunnel to Reynolds numbers representative of terminal descent at Venus.

For the geometries considered, the drag plate solidity had a negligible effect on the C_D of the model at angles of attack near 0 deg, although some dependency on solidity was evident at larger angles of attack.

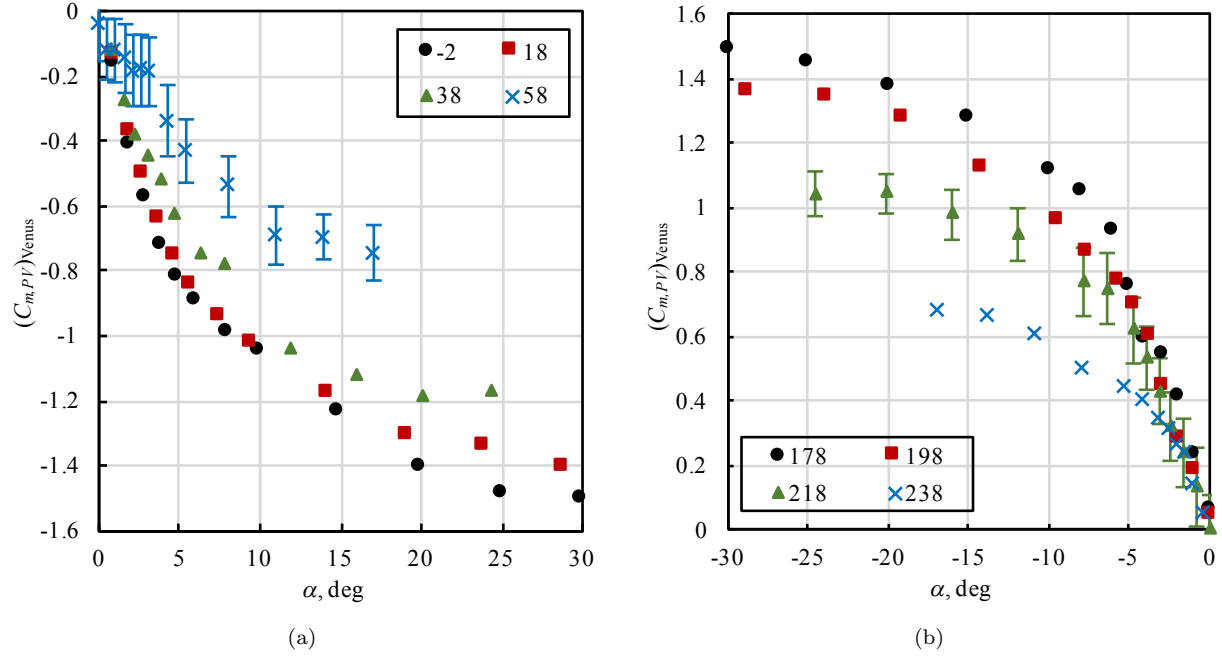


Figure 13. Extrapolated pitching moment coefficient as a function of α for the baseline VISAGE lander (83% solidity and 10 deg dihedral) at different α_T clocking angles. Error bars showing the total uncertainty (as a 95% confidence interval) for a single clocking angle are shown for reference

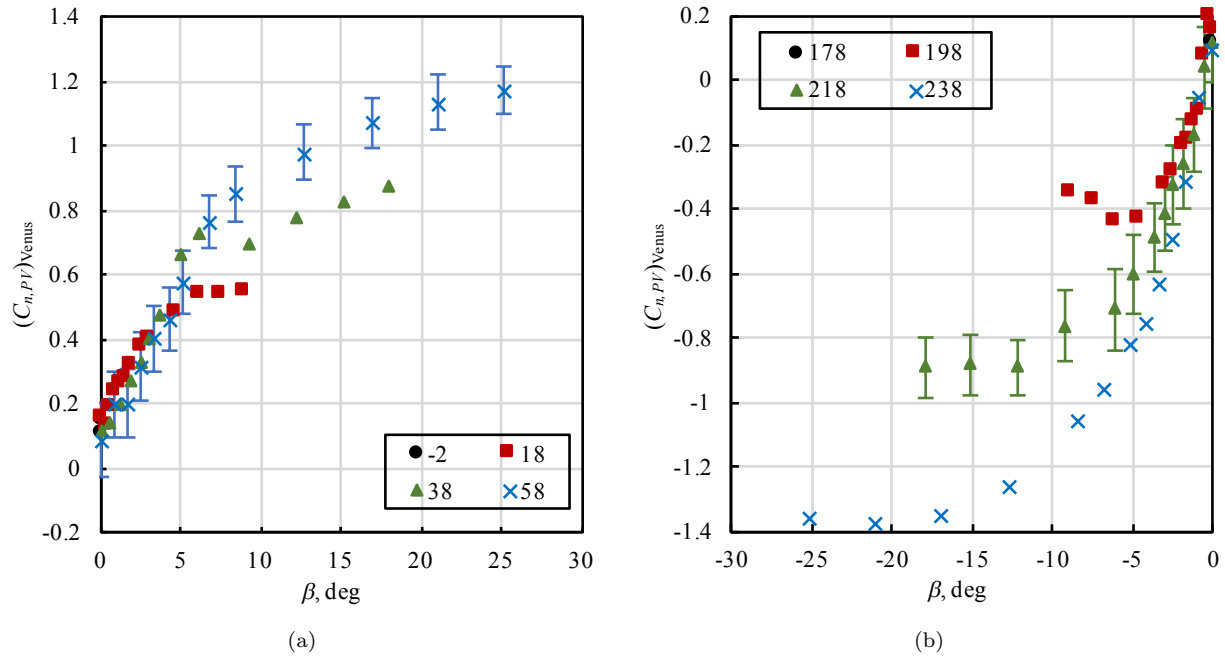


Figure 14. Extrapolated yawing moment coefficient as a function of β for the baseline VISAGE lander (83% solidity and 10 deg dihedral) at different α_T clocking angles. Error bars showing the total uncertainty (as a 95% confidence interval) for a single clocking angle are shown for reference

Note, however, that we only considered a very narrow range of solidities, and that the open area in the drag plates was located exclusively at the center of the plate. It is likely that solidity plays a more significant role in the drag performance of plates with lower overall solidity, or with different distributions of open area.

The axial, normal, and side force coefficients, as well as the pitching and yawing moment coefficients at conditions representative of terminal descent at Venus were determined as a function of angle of attack for lander models with four different drag plate configurations. All configurations were determined to be statically stable about their pitching axis (with origin at the center of the payload sphere) over the range of angles of attack considered, although the drag coefficient and degree of static stability of the models were dependent on the dihedral angle of the drag plate. In general, drag plates with larger dihedral were found to lead to increased static pitching stability about the center of the payload sphere while drag plates with smaller dihedrals were found to lead to higher axial and drag force coefficients. It should be noted that no significant difference was found between the C_A of the models tested with a flat drag plate and a plate with a 10 deg dihedral, although the latter exhibited better pitching stability. However, the configuration with the 0 deg drag plate remains statically stable, and a flat drag plate design could allow a larger drag plate to be accommodated inside the Venus entry capsule, thus improving overall drag performance.

The axial, normal, and side force coefficients, as well as the pitching and yawing moment coefficients of the lander at conditions representative of terminal descent at Venus, were also determined as a function of angle of attack and angle of sideslip for the preliminary lander design. The lander was determined to be statically stable about both their pitching and yawing axes over the range of angles of attack and sideslip considered. In addition, no significant asymmetries were identified in the aerodynamic coefficients.

The data presented here will be used to determine a preliminary database of the static aerodynamics of the preliminary VISAGE lander design, and to evaluate the impact of changes to the lander design on the aerodynamic performance of the lander and on the resulting lander descent trajectories. The present results encompass static aerodynamics only. In order to develop a high-fidelity aerodynamic database, knowledge of both static and dynamic aerodynamic coefficients is required. Therefore, dynamic wind tunnel testing of the final lander baseline design should be completed in the future.

Acknowledgments

This research was carried out at the Jet Propulsion Laboratory, California Institute of Technology, under a contract with the National Aeronautics and Space Administration. The authors gratefully acknowledge the contributions of Jeff Hall, Chris Porter, Michael Meacham, Richard Otero, and Brandon Metz at the Jet Propulsion Laboratory; of Stephanie Rider, Dimity Nelson, and Damien Hirsch at Caltech; of Karl Edquist, Soumyo Dutta, and Juan R. Cruz at the NASA Langley Research Center; and of Suman Muppidi at the NASA Ames Research Center.

References

- ¹R. S. Saunders, G. H. Pettengill, R. E. Arvidson, W. L. Sjogren, W. T. K. Johnson, and L. Pieri, L., "The Magellan Venus radar mapping mission", *Journal of Geophysical Research: Solid Earth*, 95(B6), 1990.
- ²H. Svedhem, D. V. Titov, D. McCoy, J. P. Lebreton, S. Barabash, J. L. Bertaux, and W. Markiewicz, "Venus Express—the first European mission to Venus", *Planetary and Space Science*, 55(12), 2007.
- ³L. J. Nolte and S. C. Sommer, "Probing a Planetary Atmosphere: Pioneer Venus Spacecraft Description," AIAA Paper 75-1160, 1975.
- ⁴R. Z. Sagdeev and V. I. Moroz, "Project Vega first stage: missions to Venus", *Sov. Astron. Lett.*, 12, No. 1, Jan.-Feb. 1986.
- ⁵J. R. Cruz, "Test Report for the SAGE Lander Static Wind Tunnel Test at the NASA Ames Research Center Fluid Mechanics Laboratory (FML) 48- by 32- inch Wind Tunnel ", Version 2.2, May 25, 2010.
- ⁶ATI Industrial Automation, Inc, *Six-Axis Force/Torque Sensor System Installation and Operation Manual*, Apex, NC, March, 2016.
- ⁷E. C. Maskell, "A Theory of Blockage Effects on Bluff Bodies and Stalled Wings in a Closed Wind Tunnel", Royal Aircraft Establishment, Rept. Aero 2685, Nov. 1963.
- ⁸E. C. Polhamus, "A Review of Some Reynolds Number Effects Related to Bodies at High Angles of Attack," NASA Contractor Report CR-3809, 1984.